RSC Advances

ROYAL SOCIETY OF CHEMISTRY

www.rsc.org/advances

Journal Name

ARTICLE

Perovskite as nickel catalyst precursor – Impact on catalyst stability on xylose aqueous-phase hydrogenation

Received 00th January 20xx,
Accepted 00th January 20xx

DOI: 10.1039/x0xx00000x

www.rsc.org/

Ruddy Morales[a], Cristian H. Campos[a], J.L.G Fierro[c], Marco A. Fraga[b]*, Gina Pecchi[a]*.

Precursors materials with formula mater $La_{1-x}Ce_xAl_{0.18}Ni_{0.82}O_3$ (x=0.0, 0.1, 0.5, 0.7) were successfully used as precursors to prepare Ni nanoclusters to be used as catalysts in the hydrogenation of xylose to xylitol. For the Ce free and lower Ce content (x=0.0; 0.1) the perovskite structure was obtained, whereas for higher Ce content (x=0.5; 0.7) an ordinary CeO_2-La_2O_3 solid dissolution with no perovskite structure were obtained. Under reduction conditions, the perovskite structure lead to ~30% of metallic Ni without loss of the perovskite structure (x=0.0; 0.1) and the CeO_2-La_2O_3 solid dissolution allows a Ni reduction of ~40% of Ni (x=0.5; 0.7). As expected, the similar reduced Ni content do not show large differences in the aqueous-phase xylose hydrogenation products distribution, meanwhile, the larger differences in the precursors; perovskite structure (x=0.0; 0.1) and solid dissolution (x=0.5; 0.7) point out the importance of the perovskite structure in the remarkable leaching-resistant showed by Ni perovskite-precursor (x = 0.0; 0.1) catalysts, showing no Ni leaching at all over 6 h of reaction in aqueous medium.

Introduction

Liquid phase hydrogenation of aldoses on porous metal catalyst is an important process in the synthesis of polyhydric alcohols, which have long been used as natural sweetening agents in the food industry. Xylitol, obtained by the hydrogenation of xylose, is a sweetener molecule, which has been increasingly commercialized[1] due to its attractive properties as high solubility in water, stability upon storage and do not caramelize at elevated temperatures. Moreover, the sweetening capacity of xylitol exceeds that of saccharose by 20-25% with no insulin requirement.[2,3]

Xylitol is typically produced by an isothermal hydrogenation process of xylose aqueous solutions in a triphasic batch reactor on a metallic dispersed catalyst. Wisniak et al.[3,4] studied different metal catalysts in the hydrogenation of glucose, fructose and xylose, reporting that the activity of the metals decreases in the order Ru>Ni>Rh>Pd.[2] The performance of Ni-based catalysts stands out due to their lower price compared to noble metals and that they can be efficiently used in batch reactors, with high activity and selectivity to polyalcohols. Nevertheless, the major drawback of Raney Ni catalysts is their large and fast deactivation due to accumulation of organic impurities (from the starting material) on the catalyst surface, leading to poisoning of the active sites, and metal leaching.[5] These technical hurdles motivate the pursuit of alternative catalysts by changing their chemical formulation and/or their surface architecture through different active surface site assemblies. It can be accomplished by exploring different synthesis procedures and catalyst precursors with distinctive topology or flexible crystalline structure.

Perovskite-type oxides are crystalline structures, represented by the general formula ABO_3, where A is a large cation and B is a small cation of the d-transition series. A multitude of chemical compositions is possible since a large number of chemical elements may be accommodated at both A and B positions of such flexible structure. Furthermore these crystalline structures have a large stability in oxidant atmosphere; meanwhile they can be total or partially reduced in reductive atmosphere. Due to such interesting properties, they have been extensively exploited as catalyst precursors for many reactions.[6,7] The main advantage of perovskite-like oxide as catalyst precursor is the possible formation of small and uniform particle size catalyst, which could provide a distinguished catalytic performance.

Ni-containing perovskites have been widely investigated as catalyst precursor for a broad variety of reactions. Natural gas[8] and alcohols[9] reforming, water-gas shift reaction[10], methane combustion[11] and soot oxidation[12] can be listed just to mention a few processes. In the case of $LaNiO_3$ perovskite, the reducible element (Ni^{3+}) in the perovskite structure can be easily reduced to metallic Ni° dispersed on La_2O_3 under appropriate H_2 reduction condition.[13] In hydrogenation reactions, one strategy to tailor catalyst selectivity is the employment of promoters, which can also be accommodated into perovskite catalyst precursor structure leading to a well-

[a] Departamento de Físico-Química, Facultad Ciencias Químicas, Concepción, Chile. Email: gpecchi@udec.cl
[b] Instituto Nacional de Tecnologia/MCTIC, Laboratório de Catálise, Rio de Janeiro, Brazil. Email: marco.fraga@int.gov.br
[c] Instituto Catálisis y Petroleoquímica, CSIC, 28049 Madrid, Spain.

† Supplementary Information (ESI) available: [details of any supplementary information available should be included here]. See DOI: 10.1039/x0xx00000x

dispersed system. Ceria, a well-known promoter with outstanding redox and acid-base properties, has been exploited in this regard.[14,15]

In this work, perovskite structures were investigated as a strategy to stabilize Ni nanoclusters in metal catalysts for aqueous-phase hydrogenation of xylose to xylitol. All catalyst presented a nominal Ni loading of 20 wt%, which was ensured by adding Al alongside in B position. Different Ce loadings were considered to partially substitute La in A position. A full structural and textural characterization of synthesized $La_{1-x}Ce_xAl_{0.18}Ni_{0.82}O_3$ (x=0.0, 0.1, 0.5, 0.7) structures was carried out to explain the activity and selectivity of the oxidized and reduced catalysts.

Experimental

Preparation of the catalysts

$La_{1-x}Ce_xAl_{0.18}Ni_{0.82}O_3$ (x=0.0, 0.1, 0.5, 0.7) materials, all of them with 20 wt% of nominal Ni loading and different Ce and La contents, were prepared by self-combustion method.[16] Glycine ($H_2NCH_2CO_2H$), used as ignition promoter, was added to an aqueous solution of metal nitrates with the appropriate stoichiometry to get a NO_3^-/NH_2 (molar ratio) = 1. The resulting solution was slowly evaporated until a vitreous gel was obtained. The gel was heated up to over 265°C, temperature at which the ignition reaction occurs producing a powdered precursor. After the combustion process, the powders were ground and subjected to air thermal treatment calcination to eliminate the remaining carbon and obtain the perovskite structure. Solids were crushed and sieved to obtain the required particle size (<200 μm) and then finally calcined at a heating rate of 1°C min^{-1} up to 700°C and maintained for 5 h.

Since hydrogen was used to activate the solids prior to catalytic activity measurements, the calcined perovskites were first reduced under pure hydrogen flow (50 mL min^{-1}) at 500°C for 2 h to carry out ex-situ characterization. After reduction, the reactor was purged with nitrogen, cooled down until room temperature and then placed in a cryostatic bath (a mixture of liquid nitrogen and isopropyl alcohol at –70°C). Once reached that temperature, a flow of 5% O_2/N_2 was admitted into the reactor for 1 h. Finally the bath was removed and the catalysts were stabilized at room temperature for 1 h. These materials are referred to as Ni-reduced solids hereinafter.

Samples were labeled according to their chemical composition: x=0.0 to $La_{1.0}Al_{0.18}Ni_{0.82}O_3$; x=0.1 to $La_{0.9}Ce_{0.1}Al_{0.18}Ni_{0.82}O_3$; x=0.5 to $La_{0.5}Ce_{0.5}Al_{0.18}Ni_{0.82}O_3$; x=0.7 to $La_{0.3}Ce_{0.7}Al_{0.18}Ni_{0.82}O_3$.

Characterization

Chemical analysis was conducted by atomic absorption spectrometry (AAS) using a Perkin Elmer instrument 3100. Samples were heated up in an open Teflon beaker with 2.5 mL of HNO_3, 2.5 mL of HCl and 5.0 mL of HF (all in high concentration). Once samples were dissolved, HF was evaporated to minimum volume. Finally, a spatula tip of $H_3BO_{3(s)}$ and up to 50 mL total volume of water was added in a plastic volumetric flask.

The specific areas were calculated using the BET method from the nitrogen adsorption isotherms obtained on a Micromeritics ASAP 2010 apparatus at -196°C. Samples were previously pretreated at 150°C under nitrogen atmosphere for 2 h to dehydrate and clean catalysts surface from adsorbed gases, followed by vacuum. Isotherms were recorded taking 25 relative pressure points ranging from 0.0-1.0 for adsorption and 23 for desorption process.

X-ray powder diffraction (XRD) patterns were obtained with nickel-filtered Cu$K\alpha_1$ radiation (λ=1.5418 Å) using a Rigaku diffractometer and collected in the 2θ range of 20-70° in steps of 2°C min^{-1}.

Temperature programmed reduction (TPR) experiments were performed in a TPR/TPD 2900 Micromeritics system with a thermal conductivity detector (TCD). Prior to the reduction experiments the samples (50 mg) were thermally treated under air stream at 700°C to remove any contaminants on catalysts surface. The reduction profiles were recorded under 10% H_2/N_2 flow at 25 mL min^{-1} at a heating rate of 5°C min^{-1} from room temperature to 1000°C.

NH_3-TPD experiments were carried out on the reduced samples (2 h at 500°C) on a TPR/TPD 2010 apparatus, saturating the catalyst surface at 100°C with ammonia pulses. Then the sample was cooled down to room temperature and, once the baseline was restored, the temperature linearly increased up to 500°C.

The XPS measurements were performed using a VG Escalab 200R electron spectrometer equipped with a hemispherical electron analyzer and Mg Kα (1253.6 eV) X-ray source. Prior to analysis, the samples were reduced *in situ* under hydrogen at 500°C for 1 h and transported to the analysis chamber without contact with air. Charging effects on the samples were corrected by taking the C1s peak of adventitious carbon at 284.8 eV. The peaks were decomposed into several components assuming a Gaussian/Lorentzian shape.

Catalytic activity

The catalytic activity evaluation in aqueous-phase hydrogenation of xylose was performed in a semi-batch Parr reactor at conditions (catalyst weight and agitation speed) to ensure absence of any transport limitations, evaluated by the Weisz-Prater parameter. Catalysts were reduced previous to the reaction in a conventional fixed bed reactor at 36 mL min^{-1} of H_2 and heating of 5°C min^{-1} up to 500°C and maintained at this temperature for 2 h. Afterwards, reducing gas was switched to nitrogen stream and catalyst was cooled down to room temperature.

Preliminary reaction runs were performed to settle suitable reaction conditions. A selected sample (x=0.1 catalyst) was used and reaction temperature and H_2 pressure in the reactor were systematically modified. High xylose conversion to xylitol and low secondary product formation were taken into consideration to evaluate the catalyst performance of the reaction carried out at three different experimental conditions: i) 130°C and 25 bar of H_2; ii) 100°C and 25 bar of H_2; iii) 100°C and 15 bar of H_2. Hydrogenated products were the

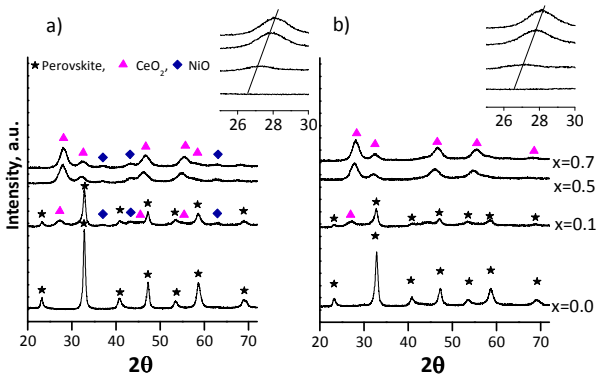

Figure 1. X-ray diffraction patterns of: a) calcined samples; b) Ni-reduced catalysts. Inset figures: enlargement of Bragg angle region corresponding to (111) plane of CeO_2.

main compounds when reaction was performed at 100°C and 25 bar of H_2, therefore, those were the operation conditions used to assess the behaviour of the synthesized samples.

In a typical run, the reactor was fed with 40 mL of water and 100 mg of catalyst, sealed and purged five times with N_2 and at last with H_2 to avoid contamination with other gases. The reactor was heated up to 100°C and stirring was set at 600 rpm. Once reached the desired temperature, 40 mL of xylose aqueous solution was admitted into the reactor, providing a starting reaction medium at 0.083 mol xylose L^{-1}. Hydrogen pressure was adjusted and kept constant at 25 bar. Samples were taken periodically during the reaction and analysed by a Waters HPLC chromatograph model Alliance e2695, coupled to a PDA detector model 2998 at wavelength of 280 nm and a RID detector model 2414 at 50°C using a Biorad Aminex HPX-87H column maintained at 65°C. H_2SO_4 aqueous solution at 5 mmol L^{-1} was used as mobile phase at 0.7 mL min^{-1}.

Total xylose conversion and product selectivity were calculated as:

$$\text{Xylose conversion} = \frac{[xilose]_i - [xilose]_t}{[Xilose]_i}$$

$$\text{Selectivity} = \frac{[product]_i}{[xilose]_i - [xilose]_t}$$

Results and Discussion

Atomic Absorption Spectrometry (AAS)

The elemental composition of Ni in the prepared solids determined by AAS is compiled in Table 1. The obtained values are similar to the nominal one (20 wt% Ni), indicating no metal loss during synthesis. For all samples, aluminium content was 1.8 wt%, added as a non-reducible element to ensure the required 20 wt% of Ni in the perovskite formulation.

X-ray diffraction (XRD)

The XRD patterns of the calcined solids shown in Figure 1a indicate significant differences in the crystalline phases as lanthanum is gradually partially substituted by cerium. Ce-free sample (x=0.0) exhibits sharp diffraction peaks indicative of a crystalline iso-structural rhombohedral $LaNiO_3$ perovskite structure (33-0711).[17] By replacing La with 6 wt% Ce (x=0.1), $LaNiO_3$ perovskite structure is maintained but segregated crystalline phases identified as fluorite CeO_2 (34-0964) and NiO (44-1159) are also formed. For larger Ce loadings (x=0.5; 0.7), the formation of a perovskite structure is no longer detected and only CeO_2 and NiO isolated phases were detected. None of the diffraction associated with lantana appeared in the XRD patterns, indicating that after calcination at 700°C this oxide phase may be highly dispersed, present as an amorphous form or incorporated into CeO_2 as solid solution.[7] This behavior is similar to that previously reported by Lima et al.[18] and Liu et al.[10] The limit of Ce loading in the A site to form a perovskite type structure is indeed ≤ 0.5, for larger Ce content a CeO_2-La_2O_3 solid solution with fluorite structure was seen to be formed. It can be noted that the diffraction peaks associated with CeO_2 fluorite structure indeed shift towards higher Bragg angles, indicative of lattice contraction (inset Fig. 1a), in line with previous result for ceria doping with other lanthanides oxides.[19,20] Considering that the ionic radii of La^{3+} (0.117 nm) is larger than Ce^{4+} (0.097 nm), the contraction of the lattice should be explained by a change into higher oxidation state of the cations releasing electrons to keep the compound neutral or additionally insertion of smaller cations, such as Ni^{3+} (0.056 nm) cation. The mean crystallite size calculated by the Debye-Scherrer equation, using the diffraction line at 2θ 32.8° for $LaNiO_3$ and 27.9° for CeO_2, indicates no large differences in the obtained d_{hkl} values. The calculated mean particle size was 15 nm for $LaNiO_3$ perovskites and 5.0 nm for CeO_2-La_2O_3 solid solution.

Table 1. Ni loading, specific area (S_{BET}) and total acidity of $La_{1-x}Ce_xAl_{0.18}Ni_{0.82}O_3$ (x=0.0, 0.1, 0.5, 0.7) samples.

Sample	%Ni*		S_{BET} (m^2g^{-1})		Total acidity
	Calcined	Post reaction	Calcined	Ni-reduced	(mmol g^{-1})
x=0.0	19	20	10	9	0.51
x=0.1	21	21	15	8	0.55
x=0.5	19	16	30	36	0.52
x=0.7	20	17	34	15	0.45

*: nominal content 20 wt%

Surface area

The surface areas shown in Table 1 display lower S_{BET} values for the x=0.0 and 0.1 perovskite type structures and larger values for those at which CeO_2-La_2O_3 solid solutions are formed (x=0.5; 0.7). Even though the S_{BET} values are similar to other perovskite type oxides,[21,22] differences in the amount of adsorbed, desorbed and the hysteresis cycle can be detected (Figure S1). According to IUPAC definition,[23] the isotherms corresponds to H3 type, characteristic of solids with slit-shaped pores, also reported for Co perovskite synthesized by self-combustion method.[22] A decrease in the specific area after reduction treatment is seen as shown in Table 1.

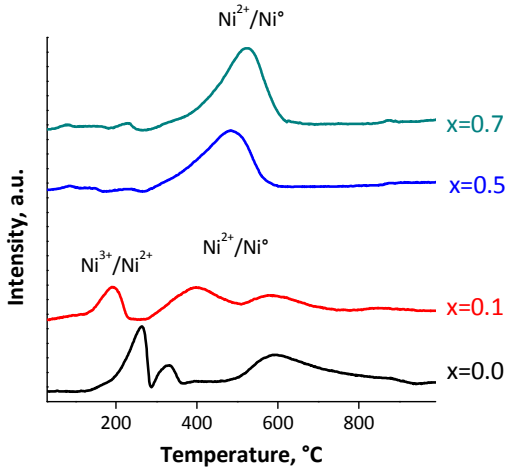

Figure 2. TPR profiles of the calcined samples.

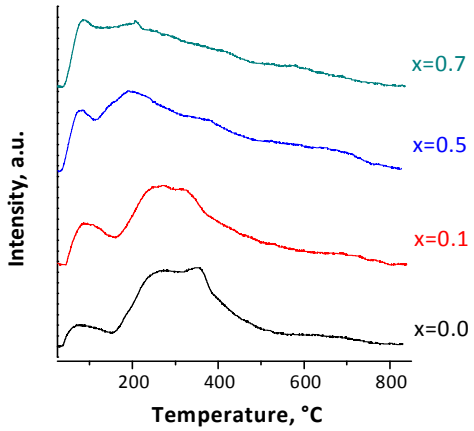

Figure 3. NH_3 desorption profiles of the Ni-reduced catalysts.

Those lower values may be explained by a sintering process upon reduction since the surface areas are almost equal to the geometrical ones as they do not possess internal microporosity.

Temperature programmed reduction (TPR)

As the main objective of this work is the preparation of stable nickel nanoclusters as chemoselective catalysts for hydrogenation of xylose to xylitol, it is of great importance to define the minimum reduction temperature to obtain reduced nickel nanoparticles without sintering. Complete reduction of non-substituted $LaNiO_3$ perovskite structure has been reported in two well-defined reduction steps; Ni^{3+} to Ni^{2+} at around 350°C followed by Ni^{2+} to Ni° at about 470°C.[10,18,24] TPR profiles of calcined materials (Figure 2) showed different reduction peaks, as it can be expected for complex systems. Taking into account that reduction of Ni^{3+} to Ni^{2+} in $LaNiO_3$ occurs at 350°C, in $LaAl_{0.18}Ni_{0.82}O_3$ (x=0.0) perovskite, the first reduction peak recorded at lower temperatures (250°C) can be assigned to the partial reduction of the perovskite structure with formation of $La_2Ni_2O_5$ [25] and $NiAl_2O_4$ [26] spinels, and the small reduction peak at 320°C can be associated to the reduction of surface OH- groups and adsorbed oxygen.[27] As for x=0.1 solid, even though same reduction peaks are seen, they are shifted to lower temperatures. Furthermore, peaks related to CeO_2 phase reduction are also seen.[17] As regarding higher Ce content (x=0.5; 0.7) samples, TPR profiles (Figure 2) show only one asymmetrical and broad reduction peak corresponding mainly to the reduction of NiO segregated on CeO_2-La_2O_3 solid solution.[28] However, CeO_2 bulk reduction could not be ruled out.[7,29] From these results, a reduction temperature of 500°C was selected for all solids, which corresponds to the temperature at which Ni reduction is starting for Ce-free perovskite (x=0.0).

This mild reduction condition leads to Ni reduction but without the complete destruction of perovskite structure, aiming at maximizing metal dispersion while avoiding Ni sintering.

Indeed, after the reduction treatment, XRD patterns of the Ni-reduced solids (Figure 1b) do not show significant differences when compared to the corresponding calcined samples.

A different behavior has been reported for $LaNiO_3$ and $La_{0.9}CeNiO_3$ perovskites elsewhere[6,8,23,24], and a complete loss of the perovskite structure was evidenced under hydrogen at 500°C forming Ni metal nanoparticles supported on a La_2O_3 matrix. Such an apparent discrepancy is indeed an important finding, which might indicate that the presence of only ~2 wt% of aluminum may avoid the destruction of the perovskite structure. At larger Ce contents (x=0.5; 0.7), reductive atmosphere does not produce any structural difference in CeO_2-La_2O_3 solid solution[30] with no sensitive effect of Al content.[6]

Ammonium temperature programmed desorption (NH_3-TPD)

The measurement of acid strength by NH_3-TPD assumes that the temperature of maximum desorption rate is a rough measure of the acid strength of the sorption sites. An acid strength distribution is thus usually proposed considering both NH_3 physically adsorbed and hydrogen-bound at ≤150°C [31] and acid site-bound NH_3 at T>150°C. Particularly it is generally accepted to classify the acid sites as i) weak (T<250°C) and moderate to strong (T>250°C) acid sites.[32]

NH_3 desorption profiles shown in Figure 3 indicate a wide distribution of acidic site strength on the surface of Ni-reduced solids. The first desorbed NH_3 peak at temperatures ≤150°C observed for all solids is attributed to physically adsorbed as previously discussed.[31] The second broad unresolved NH_3 desorption peak recorded for both x=0.0 and 0.1 Ni-reduced catalysts is similar to the supported alumina catalysts.[33] Upon Ce substitution, it is observed that for 6 wt% of Ce loading (x=0.1) almost the same TPD pattern is seen when compared to Ce free catalyst. Accordingly, only one of the strong acidic site peak at around 350°C is flattered in the x=0.1 catalyst. The total amount of desorbed NH_3 was estimated with a confidence level of 94% by deconvoluting the peaks and the data is also summarized in Table 1.

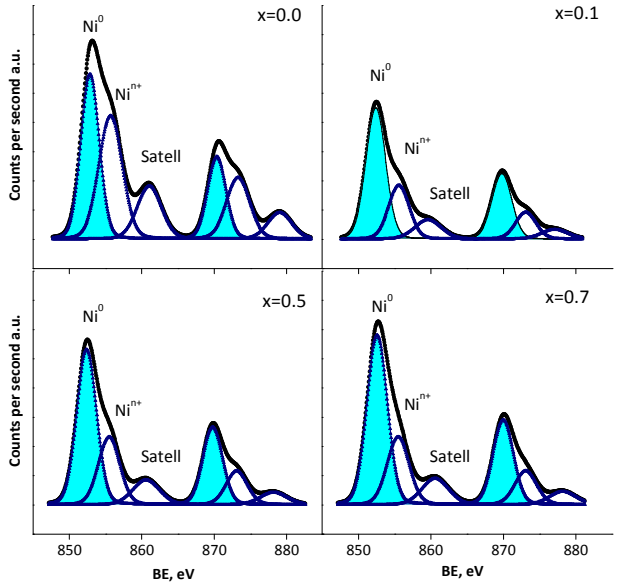

Figure 4. XPS spectra for Ni $2p_{3/2}$ for the Ni-reduced catalysts.

As it can be seen, there is no large difference in the total amount of acid sites upon Ce substitution for x≤0.5 catalysts. For the catalyst with larger substitution degree a small drop in total acidity is detected according to previous discussions where a large presence of Ce covers acid sites.

X-ray photoelectron spectroscopy (XPS)

The Ni 2p core-levels spectra for the Ni-reduced solids are shown in Figure 4, (La 3d, Ce 3d and O 1s in Figure S2) and their respective binding energies (BE) compiled in Table 2. The most intense peak of $La3d_{5/2}$ shows two components at 834.3 eV and 838.1 eV, both attributed to La^{3+}.[34,35]

A doublet followed by a satellite peak is seen for Ni $2p_{3/2}$. The first peak of the doublet is attributed to Ni°, the largest peak at 852.5±0.1 eV[36], and the second one and the satellite peak to oxidized (Ni^{2+} and Ni^{3+}) nickel species. It is not possible to distinguish between those two oxidic species due to their close BE: 857.2 eV and 856.0 eV for Ni^{2+} and Ni^{3+} [37], respectively. Ce spectra (Figure S2b) display a single peak attributed to Ce^{4+} and multiplets and satellite peaks, previously reported for Ce^{3+}.[38] The core-level spectra of Ce^{4+} and Ce^{3+} at 882.3[39] and 885.3 eV,[40] respectively, allow differentiating the surface contributions. It can be seen that the lower Ce content sample (x=0.1) shows the smallest Ce^{4+} peak, in line with previous discussion regarding the formation of a perovskite-type structure (Ce^{3+}) with presence of La_2O_3-CeO_2 (Ce^{4+}) as segregated phase in a lower extent. At larger Ce content (x=0.5; 0.7), the large increase in the core-level spectra and in the peak corresponding to the CeO_2 phase (Ce^{4+}) is also in agreement with previous characterization results.

With regard to the O1s spectra, no surface core-level spectra higher than 532 eV indicate total removal of molecular water from the surface of the samples.[41] No differences in the BE of the surface hydroxyls/carbonate groups at 531.5 eV can be seen (Table 2), meanwhile a change from 529.7 eV (x=0.5; 0.7) to 529.3 eV (x=0.0; 0.1) is detected for the lattice oxygen.

Table 2. Core levels BE (eV) of La $3d_{5/2}$, Ce $3d_{5/2}$, Ni $2p_{3/2}$ and O 1s of $La_{1-x}Ce_xAl_{0.18}Ni_{0.82}O_3$ (x=0.0, 0.1, 0.5, 0.7) reduced catalysts.

Catalyst	Binding energy (eV)			
	La $3d_{5/2}$	Ce $3d_{5/2}$	Ni $2p_{3/2}$	O 1s
x=0.0	834.3	-	852.5 (42)	529.3 (63)
			855.7 (58)	531.6 (37)
x=0.1	834.4	882.4 (79)	852.5 (61)	529.3 (64)
		885.4 (21)	855.7 (39)	531.6 (36)
x=0.5	834.3	882.6 (82)	852.4 (58)	529.7 (62)
		885.2 (18)	855.4 (42)	531.4 (38)
x=0.7	834.4	882.7 (17)	852.6 (60)	529.8 (66)
		885.6 (83)	855.5 (40)	531.5 (34)

Accordingly, this BE of O 1s for both x=0.0 and 0.1 reduced samples fits quite well the corresponding values expected for a perovskite structure,[42,43] in line with previously assigned crystalline phases as identified by XRD. Likewise the upshift to 529.7 eV for x=0.5 and 0.7 solids has been reported for oxygen species with cations in lower oxidation state,[44,45] in agreement with the shift of BE of the Ni $2p_{3/2}$ values.[44,46]

Table 3 displays the surface atomic composition and surface Ni content, calculated from the peaks at 852 eV for the Ni-reduced samples. Unfortunately, the loss of oxygen produced during reduction treatment does not allow informing the nominal ratios. The expected decrease in La/La+Ce and increase in the Ce/La+Ce upon Ce content is seen. With regard to Al/La+Ce and Ni/La+Ce ratio, the nominal values for the calcined precursors were 0.18 and 0.82 respectively; therefore much lower values in the Ni/La+Ce ratio are seen. The decrease in surface Ni content upon Ce addition is in line with XRD results regarding the contraction of ceria crystal lattice by insertion of Ni^{3+} (0.056 nm) or Ni^{2+} (0.069 nm) in CeO_2 upon reduction treatment.[47] An opposite trend observed to other reduced perovskite-type structures, where B-site cations are the ones which are surface enriched.[48,49]

Table 3. Surface atomic composition of $La_{1-x}Ce_xAl_{0.18}Ni_{0.82}O_3$ (x=0.0, 0.1, 0.5, 0.7).

Catalyst	Atomic rate				$Ni^0/Ni^{2+/3+}$	Ni*$x10^{-20}$ (at g^{-1})
	La (La+Ce)	Ce (La+Ce)	Al (La+Ce)	Ni (La+Ce)		
x=0.0	1.00	0.00	0.23	0.61	0.7	1.6
x=0.1	0.82	0.18	0.18	0.35	1.6	1.6
x=0.5	0.58	0.42	0.21	0.45	1.4	1.8
x=0.7	0.37	0.63	0.25	0.48	1.5	2.0

*nominal content of $4.1x10^{20}$ at g^{-1}

The lowest value of reduced Ni surface content (Table 3) for the Ce free Ni-reduced catalyst can be explained considering the higher thermal stability of this perovskite upon ~2 wt% aluminium insertion (Fig 3). It is proposed that the higher stability of the as-synthesized $La_{1.0}Al_{0.18}Ni_{0.82}O_3$ perovskite as well as that of $La_2Ni_2O_5$ [25] and $NiAl_2O_4$ [26] reported spinels, which would collapse when the reduction temperature reaches 600°C, does not allow to increase the concentration of surface reduced nickel at the reduction temperature of 500°C

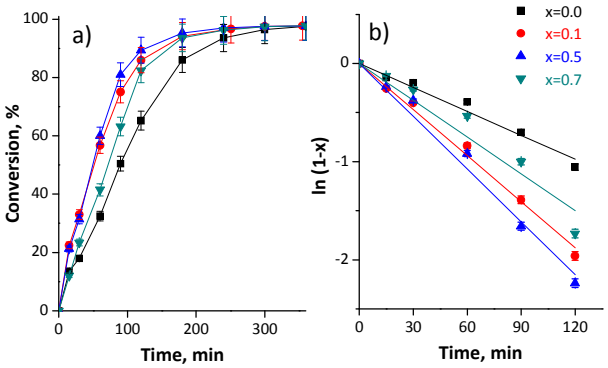

Figure 5. Xylose conversion during hydrogenation reaction at 100°C and PH_2=25 bar. a) Total conversion, b) Pseudo first order adjustment.

used for both x=0.0 and x=0.1, obtaining thus a Ni surface extent of ~30%. As concerning CeO_2-La_2O_3 solid solution precursors (x=0.5; 0.7), the reported strong metal support interaction (SMSI) effect for Ni/CeO_2 catalysts[50] is likely to explain the reducibility extent of Ni of ~36 to 40%.

Due to the lower specific surface of the Ni-reduced solids it can be extrapolated that similar surface and bulk composition would be present.[51] Therefore, considering the surface atomic composition (Table 2) and atomic ratios (Table 3), it can be possible to estimate the metallic Ni° content values. The atomic Ni^0 g^{-1} of reduced sample displayed in Table 3 will be used to the further calculate TOF as an intrinsic measurement of catalytic activity on aqueous-phase hydrogenation of xylose (Table 4).

Catalytic activity

The experimental results of total conversion and products distribution of xylose hydrogenation are depicted in Figure 5a and Figure 6, respectively. Additionally, the successfully fit of the experimental data with a pseudo first order reaction[3,4] is displayed in Figure 5b, allowing to calculate the global pseudo first order constant. The obtained values as well as the initial reaction rate, TOF values and selectivity are showed in Table 4.

Table 4. Global pseudo first order constant (kglobal), initial reaction rate (vo), TOF and xylitol selectivity of La1-xCexAl0.18Ni0.82O3 (x=0.0, 0.1, 0.5, 0.7).

Catalyst	k_{global} (min^{-1} g^{-1})	v_o (mmol L^{-1} min^{-1})	TOF (min^{-1})	$S_{xylitol}$ [a] (%)
x=0.0	0.068	4.6	1.42	39
x=0.1	0.139	6.9	2.15	35
x=0.5	0.148	7.6	2.06	39
x=0.7	0.084	5.7	1.39	51

[a] selectivity at 98% conversion.

It can be seen an increase in the global constant and reaction rate upon Ce content up to x=0.5 catalyst and a further decrease for the Ni-reduced catalyst with the larger Ce loading (x=0.7).

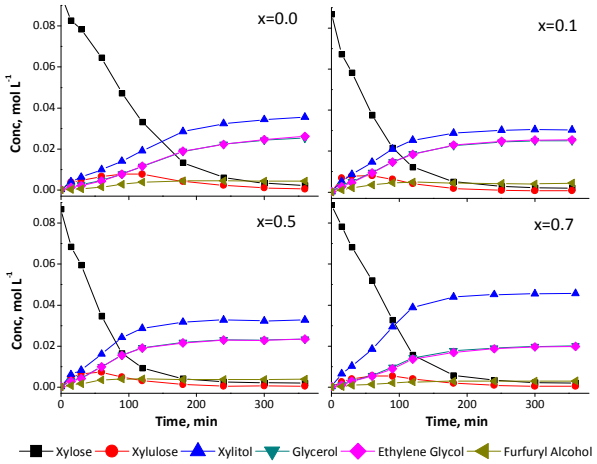

Figure 6. Products distribution during xylose hydrogenation at 100°C and PH_2=25 bar.

Selectivity to xylitol, on the other hand, did not show significant changes up to x=0.5 while an increase was seen over the sample with the highest content (x=0.7).

Regarding product distribution during reaction time, it was seen, as expected, that hydrogenation reaction is the preferred pathway, with large formation of xylitol along with ethylene glycol and glycerol. To assess the genesis of those lower carbon chain polyalcohols and infer whether they are formed straight from xylose in a parallel reaction or from xylitol hydrogenolysis as a cascade reaction, blank experiments were carried out at the same experimental conditions, but feeding the reactor with xylitol or glycerol instead of xylose.

No conversion could be observed both cases, indicating that under the experimental reaction conditions (reductive atmosphere and presence of metallic sites) xylose hydrogenation is indeed the preferential reaction route and no consecutive reactions seem to take place. It is thus proposed that xylose undergoes retro-aldol condensation to produce both glycolaldehyde and glyceraldehyde, which can be rapidly hydrogenated to ethylene glycol and glycerol, respectively.

Such a side reaction pathway has indeed been previously claimed by some authors elsewhere.[52-55] The production of these side reaction products is attributed to metallic sites promoted by basic sites.[56-60]

One should also bear in mind that Lewis acid sites can isomerise xylose to xylulose[52] and in presence of Brönsted acid sites, xylose and xylulose may produce furfural by dehydration followed by the aldehyde hydrogenation to furfuryl alcohol on metallic sites.[53] Moreover, it has been also reported that highly dispersed metallic sites closer to acid sites are able to produce furfuryl alcohol in only one step.[53] Based on the above considerations and the observed trends in the formation of xylulose and furfuryl alcohol in the experiments reported in this work (Figure 6) - xylulose reaches a maximum concentration and then consistently decreases when furfuryl alcohol is formed - a simplified reaction pathway is proposed as shown in Scheme 1.

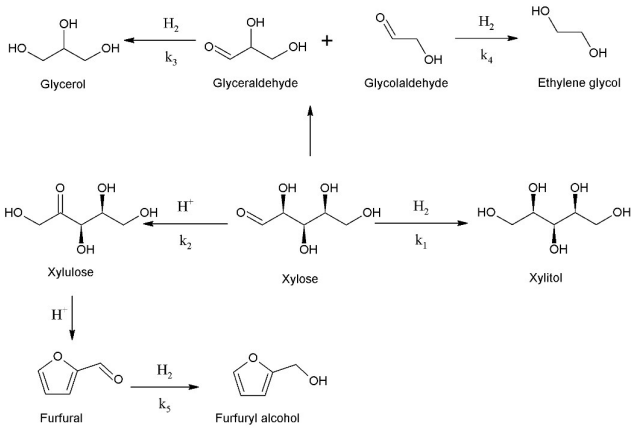

Scheme 1. Simplified reaction scheme.

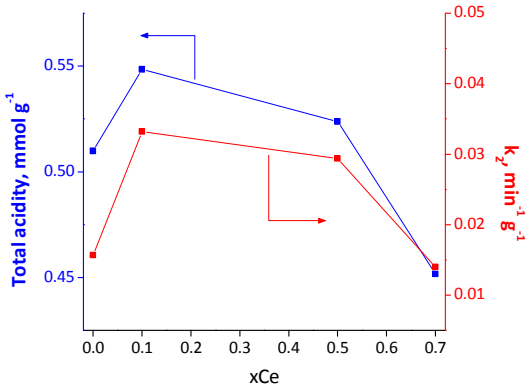

Figure 7. Total acidity and k_2 constant comparison.

According to our reaction pathway scheme, k_1, k_2, k_3 and k_4 correspond to parallel reactions steps from xylose, while k_5 represents a consecutive reaction from xylulose to furfuryl alcohol. The specific pseudo first order reaction constants for each step were calculated and are collected in Table 5. The higher values of k_1, k_3 and k_4, all corresponding to hydrogenation reactions, confirm the hydrogenation character of these catalysts. This finding is also supported by k_5 since only k_2 corresponds to a reaction (isomerisation) rather than hydrogenation. To further corroborate k_2 dependence with acidity, Figure 7 shows both total acidity and k_2 values. It can be seen that the high correlation between this curves confirm k_2 dependence upon acidity.

The turnover frequency (TOF) calculated from the surface Ni atoms as determined by XPS (Table 4) is in good agreement with some reports in the literature for Pt supported catalysts.[61] Little differences in TOF values for all the studied catalysts shows that intrinsic activity in the catalyst series is the same, without influence of neither composition nor structural differences of the catalysts. Product selectivities did not change along reaction time as revealed by the experimental data collected at 30% (Table 4) and 98% (Figure 8) isoconversion levels. Nevertheless, selectivity to xylitol increases on x=0.7 sample. This behaviour may be associated with the lower acidity of this catalyst (Table 1), which was shown to determine the reaction constant of the isomerisation reaction (Figure 7).

Table 5. Specific pseudo first order reaction constants of $La_{1-x}Ce_xAl_{0.18}Ni_{0.82}O_3$ (x=0.0, 0.1, 0.5, 0.7) reduced catalysts.

Catalyst	(min^{-1} g^{-1})				
	k_1	k_2	k_3	k_4	k_5
x=0.0	0.026	0.016	0.013	0.013	0.257
x=0.1	0.047	0.033	0.029	0.029	0.394
x=0.5	0.054	0.029	0.032	0.032	0.413
x=0.7	0.044	0.014	0.034	0.034	0.441

Indeed the k_1/k_2 ratio is expressively higher for x=0.7 catalyst (k_1/k_2=3.14) than for all the other samples with lower amounts of Ce (k_1/k_2 ranges from 1.63 to 1.86), indicating that straight hydrogenation to xylitol is preferred on this catalyst. To address one of the major drawbacks concerning the use of Ni-based catalyst in aqueous-phase hydrogenation, the studied catalysts were recovered by filtration after each batch reaction and analyzed in regard to its chemical composition, particularly Ni loading, and crystalline structure. AAS results indicate a different behaviour according to the catalyst original structure (Table 1). It can be seen that Ni content remains unchanged when the catalyst comes from a precursor holding a perovskite-type structure (x=0.0 and 0.1). On the other hand, metal leaching is evidenced for the catalysts obtained from a mixture of oxide phases (x=0.5 and 0.7). A metal loss of 15% is consistently observed for both samples, irrespective of their Ce content. This finding is quite promising since it points to a simple bottom-up approach, through a perovskite structure, able to lead to leaching-resistant catalysts.

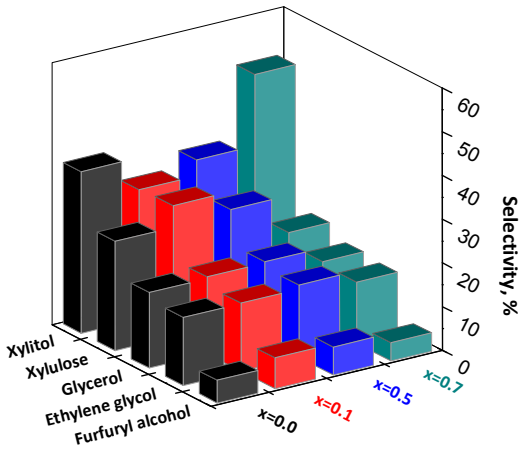

Figure 8. Selectivity to detected products at 30% of isoconversion during xylose hydrogenation. T= 100°C, PH2=25 bar.

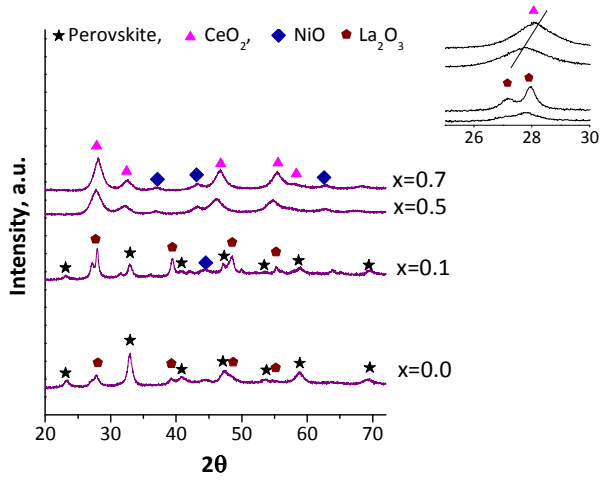

Figure 9 Post-reaction X-ray diffraction patterns. Inset figure: enlargement of region within 26 – 30° Bragg angle.

XRD patterns of all spent catalysts are displayed in Figure 9. It is noted that catalyst obtained from a bare perovskite structure (x=0.0) undergoes some structural modification upon xylose aqueous-phase hydrogenation conditions since new diffraction lines are now registered. Such peaks are associated with a crystalline La_2O_3 (22-369) isolated phase. It may have arisen from a previously highly dispersed and/or amorphous lanthanum phase not detected on the fresh sample. The presence of the perovskite structure, as evidenced by their corresponding diffraction peaks, suggests that such structure is stable, consistent with the higher metal leaching-resistance observed for this sample as already discussed. As for the other systems (x=0.1; 0.5; 0.7), no significant change was detected whatsoever, revealing, as expected, the stability of the single oxides used in the formulation.

Conclusions

$La_{1-x}Ce_xAl_{0.18}Ni_{0.82}O_3$ (x=0.0, 0.1, 0.5, 0.7) systems prepared by self-combustion method were successfully used as precursors to prepare Ni nanoclusters. Perovskite structure was obtained for Ce-free and lower Ce content samples (x=0.0; 0.1), whereas at higher Ce content (x=0.5; 0.7) a mixture of NiO and CeO_2-La_2O_3 solid solution were the main structures. All catalysts were active in aqueous-phase hydrogenation of xylose, leading mostly to xylitol and other lower carbon polyalcohols (glycerol and ethylene glycol). The highest selectivity toward xylitol was obtained on the CeO_2-La_2O_3 solid solution-supported catalyst (x=0.7) as a consequence of its lower acidity and higher activity to hydrogenation. The lower stability of this catalyst, measured as loss of Ni by leaching, spoils its use. The formation of the perovskite structure rendered remarkable leaching-resistant catalysts since no Ni loss was observed at all. Moreover, these catalysts presented only a slight lower selectivity towards xylitol production, evidencing its potential application. As the well-known Ni leaching was clear for those catalysts prepared from ordinary metal oxide phases, the promising use of perovskites as catalysts precursors for aqueous-phase processing of biomass-derived compounds is corroborated.

Acknowledgements

Authors acknowledge the support from CONICYT-Fondecyt Grant 1130005 and fellowship 21130572 (Chile) and CNPq and FAPERJ (Brazil).

Notes and references

‡ Footnotes relating to the main text should appear here. These might include comments relevant to but not central to the matter under discussion, limited experimental and spectral data, and crystallographic data.

1 T. Granström, K. Izumori and M. Leisola, *Applied Microbiology and Biotechnology*, 2007, **74**, 273.
2 J.-P. Mikkola, R. Sjöholm, T. Salmi and P. Mäki-Arvela, *Catalysis Today*, 1999, **48**, 73.
3 J. Wisniak, M. Hershkowitz, R. Leibowitz and S. Stein, *Product R&D*, 1974, **13**, 75.
4 J. Wisniak, M. Hershkowitz and S. Stein, *Product R&D*, 1974, **13**, 232.
5 M. Yadav, D. K. Mishra and J.-S. Hwang, *Applied Catalysis A: General*, 2012, **425–426**, 110.
6 N. Escalona, W. Aranzaez, K. Leiva, N. Martinez and G. Pecchi, *Applied Catalysis a-General*, 2014, **481**, 1.
7 C. A. Franchini, W. Aranzaez, A. M. Duarte de Farias, G. Pecchi and M. A. Fraga, *Applied Catalysis B: Environmental*, 2014, **147**, 193.
8 G. Valderrama, A. Kiennemann and M. R. Goldwasser, *Journal of Power Sources*, 2010, **195**, 1765.
9 S. M. de Lima, A. M. da Silva, L. O. O. da Costa, J. M. Assaf, L. V. Mattos, R. Sarkari, A. Venugopal and F. B. Noronha, *Applied Catalysis B: Environmental*, 2012, **121–122**, 1.
10 F. Liu, L. Zhao, H. Wang, X. Bai and Y. Liu, *International Journal of Hydrogen Energy*, 2014, **39**, 10454.
11 R. Hu, Y. Bai, H. Du, H. Zhang, Y. Du, J. Zhang and Q. Zhou, *Journal of Rare Earths*, 2015, **33**, 1284.
12 W. Shan, J. Yang, L. Yang and N. Ma, *Journal of Natural Gas Chemistry*, 2011, **20**, 384.
13 T. Maneerung, K. Hidajat and S. Kawi, *Catalysis Today*, 2011, **171**, 24.
14 N. Ichikawa, S. Sato, R. Takahashi and T. Sodesawa, *Journal of Molecular Catalysis a-Chemical*, 2005, **231**, 181.
15 B. C. Campo, S. Ivanova, C. Gigola, C. Petit and M. A. Volpe, *Catalysis Today*, 2008, **133**, 661.
16 L. A. Chick, L. R. Pederson, G. D. Maupin, J. L. Bates, L. E. Thomas and G. J. Exarhos, *Materials Letters*, 1990, **10**, 6.
17 Y.-J. Su, K.-L. Pan and M.-B. Chang, *International Journal of Hydrogen Energy*, 2014, **39**, 4917.
18 S. M. Lima, J. M. Assaf, M. A. Peña and J. L. G. Fierro, *Applied Catalysis A: General*, 2006, **311**, 94.
19 G. Sierra Gallego, J. Barrault, C. Batiot-Dupeyrat and F. Mondragón, *Catalysis Today*, 2010, **149**, 365.
20 A. M. Duarte de Farias, D. Nguyen-Thanh and M. A. Fraga, *Applied Catalysis B-Environmental*, 2010, **93**, 250.
21 N. Rezlescu, E. Rezlescu, P. D. Popa, C. Doroftei and M. Ignat, *Composites Part B: Engineering*, 2014, **60**, 515.
22 J. A. Villoria, M. C. Alvarez-Galvan, S. M. Al-Zahrani, P. Palmisano, S. Specchia, V. Specchia, J. L. G. Fierro and R. M. Navarro, *Applied Catalysis B: Environmental*, 2011, **105**, 276.
23 K. S. W. Sing, *Pure and Applied Chemistry*, 1982, **54**, 2201.

24 J. Choisnet, N. Abadzhieva, P. Stefanov, D. Klissurski, J. M. Bassat, V. Rives and L. Minchev, *Journal of the Chemical Society, Faraday Transactions*, 1994, **90**, 1987.
25 M. E. Rivas, C. E. Hori, J. L. G. Fierro, M. R. Goldwasser and A. Griboval-Constant, *Journal of Power Sources*, 2008, **184**, 265.
26 C. H. Campos, P. Osorio-Vargas, N. Flores-Gonzalez, J. L. G. Fierro and P. Reyes, *Catal Lett*, 2016, **146**, 433.
27 L. G. Tejuca, J. L. G. Fierro and J. M. D. Tascón, in *Advances in Catalysis*, eds. H. P. D.D. Eley and B. W. Paul, Academic Press, 1989, vol. Volume 36, pp. 237.
28 P. Osorio-Vargas, C. H. Campos, R. M. Navarro, J. L. G. Fierro and P. Reyes, *Journal of Molecular Catalysis a-Chemical*, 2015, **407**, 169.
29 H. Zhu, W. Wang, R. Ran and Z. Shao, *International Journal of Hydrogen Energy*, 2013, **38**, 3741.
30 X. Han, Y. Yu, H. He and W. Shan, *International Journal of Hydrogen Energy*, 2013, **38**, 10293.
31 D. Liu, P. Yuan, H. Liu, J. Cai, D. Tan, H. He, J. Zhu and T. Chen, *Applied Clay Science*, 2013, **80–81**, 407.
32 J. A. Cecilia, A. Infantes-Molina, E. Rodriguez-Castellon, A. Jimenez-Lopez and S. T. Oyama, *Applied Catalysis B-Environmental*, 2013, **136**, 140.
33 K. Jiratova, A. Spojakina, L. Kaluza, R. Palcheva, J. Balabanova and G. Tyuliev, *Chinese Journal of Catalysis*, 2016, **37**, 258.
34 B. Kucharczyk and W. Tylus, *Catalysis Today*, 2004, **90**, 121.
35 B. Kucharczyk and W. Tylus, *Applied Catalysis A: General*, 2008, **335**, 28.
36 J. C. Klein and D. M. Hercules, *Journal of Catalysis*, 1983, **82**, 424.
37 S. M. d. Lima, M. A. Peña, J. L. G. Fierro and J. M. Assaf, in *Studies in Surface Science and Catalysis*, eds. M. S. Fábio Bellot Noronha and S.-A. Eduardo Falabella, Elsevier, 2007, vol. Volume 167, pp. 481.
38 P. S. Bagus, C. J. Nelin, Y. Al-Salik, E. S. Ilton and H. Idriss, *Surface Science*, 2016, **643**, 142.
39 E. Paparazzo, G. M. Ingo and N. Zacchetti, *Journal of Vacuum Science & Technology A*, 1991, **9**, 1416.
40 Y. Ohno, *Physical Review B*, 1993, **48**, 5515.
41 L. G. Tejuca, J. L. G. Fierro and J. M. D. Tascon, *Advances in Catalysis*, 1989, **36**, 237.
42 L. G. Tejuca and J. L. G. Fierro, *Thermochimica Acta*, 1989, **147**, 361.
43 R. P. Vasquez, *Surface Science Spectra*, 1992, **1**, 361.
44 N. S. McIntyre and M. G. Cook, *Analytical Chemistry*, 1975, **47**, 2208.
45 G. C. Allen and K. R. Hallam, *Applied Surface Science*, 1996, **93**, 25.
46 V. A. M. Brabers, F. M. van Setten and P. S. A. Knapen, *Journal of Solid State Chemistry*, 1983, **49**, 93.
47 R. Pereñíguez, V. M. González-DelaCruz, J. P. Holgado and A. Caballero, *Applied Catalysis B: Environmental*, 2010, **93**, 346.
48 G. Pecchi, C. M. Campos, M. G. Jiliberto, E. J. Delgado and J. L. G. Fierro, *Applied Catalysis A: General*, 2009, **371**, 78.
49 G. Pecchi, P. Reyes, R. Zamora, L. E. Cadus and J. L. G. Fierro, *Journal of Solid State Chemistry*, 2008, **181**, 905.
50 A. Caballero, J. P. Holgado, V. M. Gonzalez-delaCruz, S. E. Habas, T. Herranz and M. Salmeron, *Chemical Communications*, 2010, **46**, 1097.
51 R. Dinamarca, C. Sepúlveda, E. J. Delgado, O. Peña, J. L. G. Fierro and G. Pecchi, *Journal of Catalysis*, 2016, **338**, 47.
52 V. Choudhary, S. Caratzoulas and D. G. Vlachos, *Carbohydrate Research*, 2013, **368**, 89.
53 R. F. Perez and M. A. Fraga, *Green Chemistry*, 2014, **16**, 3942.
54 J.-P. Mikkola, T. Salmi and R. Sjöholm, *Journal of Chemical Technology & Biotechnology*, 1999, **74**, 655.
55 D. K. Mishra, A. A. Dabbawala and J.-S. Hwang, *Journal of Molecular Catalysis A: Chemical*, 2013, **376**, 63.
56 J. Lee, Y. Xu and G. W. Huber, *Applied Catalysis B: Environmental*, 2013, **140–141**, 98.
57 N. Li and G. W. Huber, *Journal of Catalysis*, 2010, **270**, 48.
58 J. Sun and H. Liu, *Green Chemistry*, 2011, **13**, 135.
59 J. Sun and H. Liu, *Catalysis Today*, 2014, **234**, 75.
60 K. Wang, M. C. Hawley and T. D. Furney, *Industrial & Engineering Chemistry Research*, 1995, **34**, 3766.
61 A. Tathod, T. Kane, E. S. Sanil and P. L. Dhepe, *Journal of Molecular Catalysis A: Chemical*, 2014, **388–389**, 90.

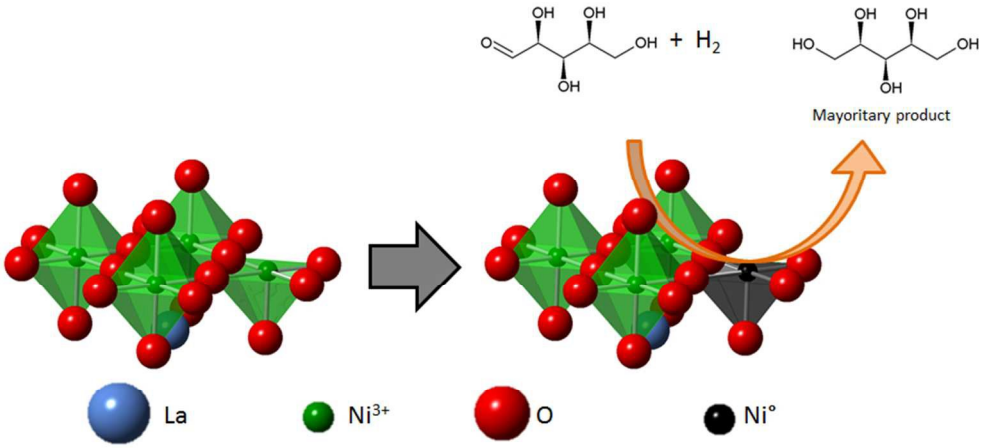

237x124mm (96 x 96 DPI)